

Cohesive zone modelling of cracked interface

Sriram H

A Thesis Submitted to
Indian Institute of Technology Hyderabad
In Partial Fulfillment of the Requirements for
The Degree of Master of Technology



Department of Mechanical and Aerospace Engineering

July 2015

Declaration

I declare that this written submission represents my ideas in my own words, and where ideas or words of others have been included, I have adequately cited and referenced the original sources. I also declare that I have adhered to all principles of academic honesty and integrity and have not misrepresented or fabricated or falsified any idea/data/fact/source in my submission. I understand that any violation of the above will be a cause for disciplinary action by the Institute and can also evoke penal action from the sources that have thus not been properly cited, or from whom proper permission has not been taken when needed.

Sriram

(Signature)

(Sriram H)

ME13M1015

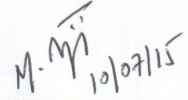
(Roll No.)

Approval Sheet

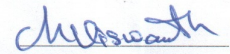
This Thesis entitled Cohesive zone modelling of cracked interface by Sriram H is approved for the degree of Master of Technology from IIT Hyderabad



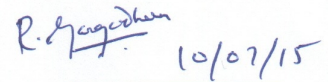
(Dr. S Suriya Prakash) Examiner
Asst. Professor
Dept. of Civil Engg.
Indian Institute of Technology, Hyderabad



(Dr. Ramji M) Examiner
Associate Professor
Dept. of Mech Engg.
Indian Institute of Technology, Hyderabad



(Dr. Viswanath Chinthapenta) Adviser
Asst. Professor
Dept. of Mech Engg.
Indian Institute of Technology, Hyderabad



(Dr. Gangadharan) Chairman
Asst. Professor
Dept. of Mech Engg.
Indian Institute of Technology, Hyderabad

Acknowledgements

I would first like to thank my parents for their unconditional support through all the times. I would like to thank Dr. Viswanath Chinthapenta for his suggestions and advice during my thesis work. I would also like to thank my grandmother, K Meena, up in the heavens, for always having believed in me. I would like to thank Anwar Sadath and Harilal R for their support and timely advice during my time at IIT Hyderabad, right from the start.

The help rendered by lab mates Jistom and Rajesh Kumar Meena were invaluable in the completing of this document. Last but not least I would like to thank god almighty for his blessings and grace during all times. The help given by Milind Tand Yogesh Wagh were instrumental in the completion of the thesis.

Dedication

To my parents, my brother and my grandmother

Abstract

A numerical study of the cohesive zone behavior under static and dynamic loading is conducted for a Mode III problem. We consider a compact tension specimen for the numerical study and the crack was modelled with several different cohesive zone models such as triangular and bilinear. The elements were formatted with the cohesive elements in the element library of the commercially available software ABAQUS. The crack growth characteristics for different material models i.e. linear elastic and elasto-plastic are compared for both the static and dynamic crack growth. The J-Integral values are compared for each of the models. The J integral values for the different CZ models were found to be almost same for the different cohesive models.

Contents

Acknowledgements	iv
Abstract	vi
Nomenclature	viii
1 Introduction and Literature review	4
1.1 Motivation	4
1.2 Objective	4
1.3 Literature Review	4
1.4 Outline of the thesis	6
2 Basics of Fracture mechanics	7
2.1 Introduction	7
2.1.1 Different types of loading	7
2.2 A study of crack propagation	8
2.2.1 Linear elastic fracture mechanics	8
2.2.2 Elasto plastic fracture mechanics	10
3 Cohesive zone modelling of cracked interface	15
3.1 Cohesive Model	15
3.2 Modelling	17
3.2.1 Specimen geometry	17
3.2.2 Finite Element Model	18
3.2.3 Cohesive element	19
3.2.4 Loading	21
3.2.5 Results	21
3.3 Conclusion and Future Scope	22
4 Crack propagation in bimaterial using spectral methods	24
4.1 Introduction	24
4.1.1 Bimaterial interface	25
4.1.2 Problem Description	25
4.2 Formulation	25
4.2.1 Two-dimensional formulation	26
4.2.2 Spectral Formulation for Mode III	27

4.2.3	Independent Formulation	28
4.3	Numerical procedure	30
4.3.1	Cohesive model	30
5	Quantification of crack tip parameters using DIC	31
5.1	Introduction	31
5.2	Digital Image Correlation	32
5.2.1	Displacement Mapping	32
5.3	Experimental Procedure	33
5.4	Experimental Setup: DIC	35
5.5	Fracture Parameters Estimation using Analytical and Numerical Modelling	36
5.5.1	Analytical Approach	36
5.5.2	J-Integral	36
5.5.3	Crack Tip Opening Displacement(δ)	37
5.6	Numerical analysis	38
5.7	Results	38
5.7.1	Analytical Results	38
5.7.2	Experimental results	39
5.7.3	Numerical analysis results	40
5.8	Conclusion	41
	References	43

List of Figures

2.1	Mode I fracture	7
2.2	Mode II fracture	8
2.3	Mode III fracture	8
2.4	K dominated zone	9
2.5	Stress distribution for different types of loading	10
2.6	J Integral	11
2.7	Plate with a crack subjected to a tensile stress [1]	12
2.8	Driving force vs. R curve diagram [1]	13
3.1	The strip yield model [1]	15
3.2	Crack tip cohesive model	16
3.3	Different forms of traction-separation law	16
3.4	Cohesive zone	17
3.5	Cohesive element	17
3.6	Subset matching and deformation tracking in DIC	18
3.7	Cohesive interaction specified at the point of contact	19
3.8	Expreimental Elasto-Plastic stress strain curve	19
3.9	Mesh used in crack analysis	20
3.10	Traction separation law for cohesive elements	20
3.11	Linear traction separation law	20
3.12	Loading for Mode III	21
3.13	Stress plots for Mode III-LEFM The computed J-Integral value was 13.69 kJ/mm^2 .	21
3.14	Stress plots for Mode III-EPFM The computed J-Integral value was 17.38 kJ/mm^2	22
3.15	Stress plots for Mode III-Dynamic The computed J-Integral value was 15.87 kJ/mm^2	22
4.1	Bimaterial subjected to Anti-plane shear	25
4.2	Convolution kernel plot for mode III	29
4.3	Cohesive Element	30
5.1	Subset matching and deformation tracking in DIC	32
5.2	Speckled image pattern in CT specimen	33
5.3	Subset matching and deformation tracking in DIC	34
5.4	Expreimental Elasto-Plastic stress strain curve	34
5.5	Experimental setup	35
5.6	Loaded CT specimen	35

5.7	J Integral	37
5.8	Meshed CT specimen	39
5.9	Load vs. CMOD	39
5.10	Strain plot obtained form FE software	40
5.11	Strain plots from DIC	40
5.12	J Integral vs Ligament length	41
5.13	Load vs COD	41

List of Tables

2.1	Stress fields ahead of crack tip for mode I and mode II	9
2.2	Crack tip opening displacement fields for Mode I and Mode II	10
2.3	Stress and displacement or mode III	10
3.1	CT specimen dimensions with edge crack	18
3.2	J integral values at different conditions for linear cohesive zone model	21
3.3	J integral values at different conditions for bilinear CZ model	22
5.1	CT specimen dimensions with edge crack	33
5.2	Material properties obtained from elasto-plastic stress-strain curve	35
5.3	Fracture parameters for Al T6 531 edge cracked CT specimen	42

Chapter 1

Introduction and Literature review

1.1 Motivation

The advances in computational tools and capabilities have made it possible to study crack propagation in various materials. These advances can help predict the failure of the structures. Among the advances in fracture mechanics, the cohesive zone model has been used widely for studying crack propagation. Cohesive zone models are a powerful tool to describe the separation of material ahead of crack tip. The cohesive zone models are used to describe the failure in various materials like ceramics, concrete, polymers.

The cohesive zone model (CZM) offers an alternative way to view the failure through materials and along material interfaces. It is a phenomenological model rather than an exact physical representation of the material behaviour of the fracture process zone. The cohesive zone model can be viewed as an alternative method to model separation [2]. The cohesive zone model describes the fracture of materials at a physical level. The CZM also eliminates the singularity of the stresses and limits it to the prescribed cohesive strength of the material. Thus, the cohesive zone model is an ideal framework to model failure, stiffness and strength in many different materials which makes the study essential.

1.2 Objective

To conduct a numerical study of the cohesive zone behaviour under static and dynamic loading for a mode III problem. The study is to be conducted using a numerical model for a compact tension specimen. The study was conducted for two different cohesive zone models such as triangular and bilinear models. The crack growth characteristics for different material models i.e linear elastic and elasto-plastic are to be compared for both static and dynamic crack growth.

1.3 Literature Review

Raman P Singh and Venkitanarayanan Parameswaran [3] studied the dynamic crack propagation in a brittle material reinforced with a ductile layer. They coupled dynamic photoelasticity with the help of digital high speed photography and the displacement and load histories were obtained using

a Hopkinson bar. The used ductile Aluminium between two thick layers of brittle Homalite-100, this single edge-notched specimen was loaded in three point bending .

Xiangting Su et al. [4] proposed an algorithm for embedding cohesive elements in ABAQUS to model cracks in a 3D model in quasi brittle material. C Guo and C T [5] Sun studied the dynamic crack propagation in a composite to study the crack propagation at various speeds. A study on the cohesive element library in ABAQUS was conducted by Daniel W Spring and Glaucio H Paulino [6]. C A Sciammarella and Oliver Combel conducted an elasto-plastic analysis on the crack tip fields in a compact tension (CT) specimen [7]. A crack closure analysis was conducted by Y Lei [8] on a CT specimen using FE analysis. An experimental and numerical study on the dynamic fracture of a concrete compact tension specimen was studied by Josko Osbolt et al. [9]. They observed crack branching at approximately a speed of $800m/s$. This can be attributed to the rate dependent behavior of concrete.

A Turon et al. [10] have proposed a method for determining the size of the cohesive finite element and length of the cohesive zone for the correct dissipation of energy. The analytical solutions for cohesive zone models for a few sample problems have been solved by J G Williams and H Hadavinia [11]. Viggo Tvergaard [12] has used the cohesive zone model to predict the crack growth in ductile fracture. He has used special interface elements ahead of the crack tip for studying the fracture behaviour. H Li and N Chandra [13] have studied crack initiation and crack growth resistance in elastic plastic materials dominated by crack tip plasticity. They have used two different types of cohesive zone models i.e exponential and bilinear models to represent the mechanical behaviour. Experimental procedures have been developed by Alfred Cornec et al. [14] for the prediction of cohesive stress and cohesive energy. They have used these parameters to propose a specific traction separation law.

I Scheider et al. [15] have compared two different numerical models on their ability to predict the ductile crack extension in thin aluminium sheets. They used the cohesive model and the R curve based on the CTOA (crack tip opening angle). They compared the respective models with the experimental values. An analysis of the crack growth in a thin sheet metal has been conducted by Weizhou Li and Thomas Siegmund [16] using the cohesive zone model. The cohesive zone model has also been used by I Scheider and W Brocks [17] for simulating the cup and cone fracture. They have concluded that the model is able to predict the failure mechanism i.e normal fracture at the center and the shear fracture at the specimen rim. Viggo Tvergaard [18] has studied the ductile fracture for mixed mode interface crack growth using the cohesive zone models. He has also done a separate study on the failure between rigid and elastic solids using a cohesive zone model [19].

W Zhang and X Deng [20] have studied an interfacial crack with a cohesive zone ahead of crack tip. They used the cohesive zone method to study a linearly elastic isotropic bimaterial to study the mixed mode asymptotic stress and displacement fields around crack tip under plane deformation conditions. The same group of scientists have also derived using elliptical coordinates, the asymptotic stress and displacement fields near the cohesive zone of a Mode III crack that is normal to a bimaterial interface [21]

1.4 Outline of the thesis

Chapter 1: The chapter deals with the introduction and the literature survey. It begins with the motivation as to why the study on cohesive zone models is important. And moves on to the objective and finally concludes with the present research in the field of cohesive zone modelling.

Chapter 2: The chapter involves a brief study on the basics of fracture mechanics and the major definitions and terms associated with it, which are necessary for the studies.

Chapter 3: This chapter outlines the procedure followed for studying the different cohesive zone models. A brief description of cohesive zone models is given and the modelling procedures for the study is also outlined in the chapter.

Chapter 4: The chapter describes the progress in the study of the delamination in bimaterial using spectral methods. A description of the formulation is given in this chapter.

Chapter 5: The final chapter describes the study on "Quantifying crack tip displacements using DIC". It describes the experimental, analytical and numerical procedure followed for studying the crack propagation in a compact tension specimen using digital image correlation. The values of J-integral, stress intensity factors and crack tip opening displacements obtained from the different methods were compared.

Chapter 2

Basics of Fracture mechanics

2.1 Introduction

Fracture mechanics deals with the study of propagation of cracks in materials. In fracture mechanics, our main attention is focused on how cracks grow subject to various external factors. Fracture is a problem faced by society for as long as structures have been in existence. This chapter describes the basics of fracture mechanics.

2.1.1 Different types of loading

There are three different modes of loading that are present in cracks. They are based on the various methods in which the crack grows. Crack initiation and propagation accompany the fracture. The mode I crack or the opening mode in which a tensile force acts normal to the plane of the crack. The mode II crack or the sliding mode where a shear stress acts parallel to the plane of the crack and is perpendicular to the crack front. The mode III crack or the tearing mode where a shear stress acts parallel to the plane of the crack and parallel to the crack front. The Figures (2.1, 2.2, 2.3) shows the three different types of loading.

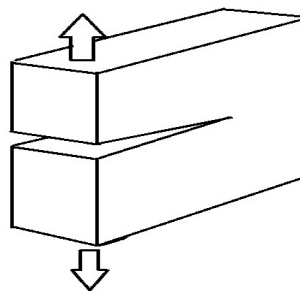


Figure 2.1: Mode I fracture

The three types of loading that are applied to enable a crack to propagate

- 1.Mode I : A tensile force is applied normal to the plane of the crack (Fig. 2.1)
- 2.Mode II : A shear stress is applied parallel to the plane of the crack and perpendicular to the crack front(Fig. 2.2).

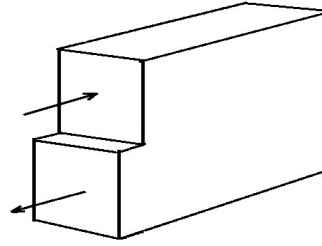


Figure 2.2: Mode II fracture

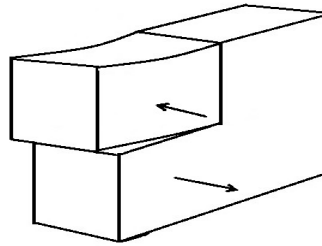


Figure 2.3: Mode III fracture

3.Mode III: A shear stress acting parallel to the plane of the crack and parallel to the crack front(Fig. 2.3).

2.2 A study of crack propagation

2.2.1 Linear elastic fracture mechanics

The domain of linear elastic fracture mechanics (LEFM), whose concepts were derived before 1960, are applicable to materials which follow Hooke's law. The LEFM is a basic theory of fracture that deals with cracks in elastic bodies i.e the material is assumed to be linear elastic and isotropic. The theory is applied for materials that are elastic except along a small region around the crack tip. It assumes small scale yielding, where the inelastic deformation is small compared to the size of the crack. In case of small scale yielding, the stress intensity factor (K) and the J integral characterize the crack tip condition. The stress distribution is proportional to the $\frac{1}{\sqrt{r}}$. The K dominated zone is shown in the Fig. 2.4.

Stress states for mode I,II and III cracks

The load types are classified into three different modes as Mode I, II and III. Mode I is an opening tensile mode, mode II is a sliding mode(in-plane shear) and mode III is tearing mode(anti-plane shear). In mode I loading the principal load is applied normal to the crack plane, tends to open the crack. Mode II corresponds to in-plane shear loading and tends to slide one crack face with respect

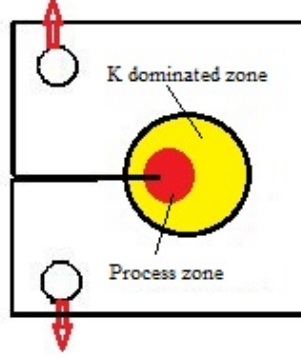


Figure 2.4: K dominated zone

to the other. Mode III refers to out-of-plane shear. A cracked body can be loaded in any one of these modes, or a combination of two or three modes.

The stress intensity factor (SIF) K , is used in fracture mechanics to compute the stress state near the crack tip. The stress state exists due to an external load (far field). The stress state is also caused due to residual stresses. The magnitude of SIF distribution depends on the geometry of the sample, the crack length and also the distribution of loads in the material. Each mode of loading produces a $\frac{1}{\sqrt{r}}$ singularity. The stress field ahead of crack tip is as given in equation

$$\sigma_{ij}^I = \frac{K_I}{\sqrt{2\pi r}} f_{ij}(\theta) \quad (2.1)$$

$$\sigma_{ij}^{II} = \frac{K_{II}}{\sqrt{2\pi r}} f_{ij}(\theta) \quad (2.2)$$

$$\sigma_{ij}^{III} = \frac{K_{III}}{\sqrt{2\pi r}} f_{ij}(\theta) \quad (2.3)$$

The Linear Elastic Fracture Mechanics (LEFM) assumptions are not accurate near the crack tip where the material non-linearities and other effects play an important role. So the true stress-strain distributions will have 3 general regions. The process zone which is close to the crack tip where the material has suffered irreversible damage. The second region where the Linear elastic assumption is accurate. The region is called region of K dominance. The third region where the crack does not influence the stress distribution (as in Fig. 2.4). The stress field for different modes are described in Tab. (2.1, 2.2, 2.3)

Table 2.1: Stress fields ahead of crack tip for mode I and mode II

Quantity	Mode I	Mode II
σ_{xx}	$\frac{K_I}{\sqrt{2\pi r}} \cos(\frac{\theta}{2}) [1 - \sin(\frac{\theta}{2}) \sin(\frac{3\theta}{2})]$	$-\frac{K_{II}}{\sqrt{2\pi r}} \sin(\frac{\theta}{2}) [2 + \cos(\frac{\theta}{2}) \cos(\frac{3\theta}{2})]$
σ_{yy}	$\frac{K_I}{\sqrt{2\pi r}} \cos(\frac{\theta}{2}) [1 + \sin(\frac{\theta}{2}) \sin(\frac{3\theta}{2})]$	$\frac{K_{II}}{\sqrt{2\pi r}} \sin(\frac{\theta}{2}) \cos(\frac{\theta}{2}) \cos(\frac{3\theta}{2})$
τ_{xy}	$\frac{K_I}{\sqrt{2\pi r}} \cos(\frac{\theta}{2}) \sin(\frac{\theta}{2}) \cos(\frac{3\theta}{2})$	$\frac{K_{II}}{\sqrt{2\pi r}} \cos(\frac{\theta}{2}) [1 - \sin(\frac{\theta}{2}) \sin(\frac{3\theta}{2})]$
σ_{zz}	0 (Plane stress), $\nu(\sigma_{xx} + \sigma_{yy})$ (Plane strain)	0 (Plane stress), $\nu(\sigma_{xx} + \sigma_{yy})$ (Plane strain)

ν is the Poisson's ratio

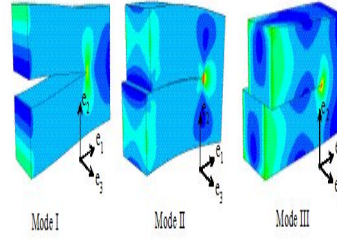


Figure 2.5: Stress distribution for different types of loading

Table 2.2: Crack tip opening displacement fields for Mode I and Mode II

Quantity	Mode I	Mode II
u_x	$\frac{K_I}{2\mu} \sqrt{\frac{r}{2\pi}} \cos\left(\frac{\theta}{2}\right) [\kappa - 1 + 2 \sin^2 \frac{\theta}{2}]$	$\frac{K_{II}}{\mu} \sqrt{\frac{r}{2\pi}} \cos\left(\frac{\theta}{2}\right) [\kappa + 1 + 2 \cos^2 \frac{\theta}{2}]$
u_y	$\frac{K_I}{2\mu} \sqrt{\frac{r}{2\pi}} \sin\left(\frac{\theta}{2}\right) [\kappa - 1 + 2 \cos^2 \frac{\theta}{2}]$	$-\frac{K_{II}}{2\mu} \sqrt{\frac{r}{2\pi}} \cos\left(\frac{\theta}{2}\right) [\kappa - 1 - 2 \sin^2 \frac{\theta}{2}]$

Where μ is the shear modulus

$$\kappa = 3 - 4\nu \text{ (plane strain)}$$

$$\kappa = \frac{3-\nu}{1+\nu}$$

Table 2.3: Stress and displacement or mode III

Quantity	Mode III
τ_{xz}	$-\frac{K_{III}}{\sqrt{2\pi r}} \sin \frac{\theta}{2}$
τ_{yz}	$\frac{K_{III}}{\sqrt{2\pi r}} \cos \frac{\theta}{2}$
u_z	$\frac{K_{III}}{\mu} \sqrt{\frac{r}{2\pi}} \sin\left(\frac{\theta}{2}\right)$

2.2.2 Elasto plastic fracture mechanics

As mentioned earlier, the domain of LEFM only extends to small scale yielding. However, these theories cannot be applied to many of the cases. The elasto plastic fracture mechanics is applied to materials that exhibit time dependent plastic behavior. The J integral and the CTOD (Crack tip opening displacement) are used to characterize crack tip plastic conditions.

Linear elastic stress analysis of sharp cracks predicts infinite stresses at the crack tip. In real materials, however, stresses at the crack tip are finite because the crack-tip radius must be finite. Inelastic material deformation, such as plasticity in metals and crazing in polymers, leads to further relaxation of crack-tip stresses. The elastic stress analysis becomes increasingly inaccurate as the inelastic region at the crack tip grows. Simple corrections to linear elastic fracture mechanics (LEFM) are available when moderate crack-tip yielding occurs. For more extensive yielding, one must apply alternative crack tip parameters that take nonlinear material behavior into account.

J Integral

The domain of LEFM cannot accurately capture the elasto-plastic fracture behaviour. Hence, based on the small scale yielding , J R Rice [22] in 1968 proposed a new fracture parameter called as J-integral. The magnitude of J-integral represents the non-linear energy release rate due to crack. They have also shown that J-integral is path independent. Hence, it can be evaluated for any path for given loading condition and its functional form is expressed in Eq. 2.4 The schematic in Fig. 2.6 represents a typical edge crack under uniaxial loading with a contour .

$$J = \oint_{\tau} (W dy - T_i \frac{\partial u_i}{\partial x} ds) \quad (2.4)$$

Where, W is the strain energy density, T_i is the component of traction vector, and τ is closed contour. For estimating J it is separated into elastic and plastic components [1] as shown in Eqn 2.5

$$J = J_{pl} + J_{el} \quad (2.5)$$

The crack tip energy integral is path independent as the material enclosed by the contour is homogeneous. For elastic solids, $J_{el} = G$ contour integral gives the crack tip energy release rate [23]

$$J_{pl} = \frac{\eta_{pl} A_{pl}}{Bb}, \quad \eta_{pl} = 2 + 0.522 * \frac{b}{W} \quad (2.6)$$

Here η_{pl} is the plastic eta factor, B is the specimen thickness, A_{pl} is the area under the Load- CMOD curve, b is the un-crack length, W is the width of the specimen.

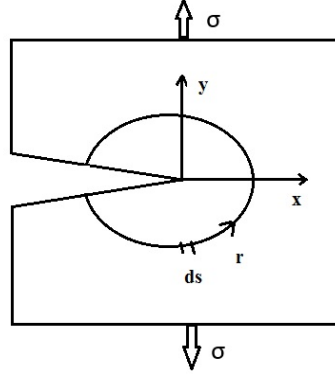


Figure 2.6: J Integral

$$J_{el} = G = \frac{K_I^2}{E'} \quad (2.7)$$

Where, E is Young's modulus and μ is Poisson's ratio

Nonlinear Energy release rate

Griffith proposed an energy balance criterion for the propagation of crack in a plate. A plate with a crack of length $2a$ is considered (see Fig. 2.7), for the crack to undergo an extension, sufficient energy must be provided or available to overcome the surface energy of the material. The energy

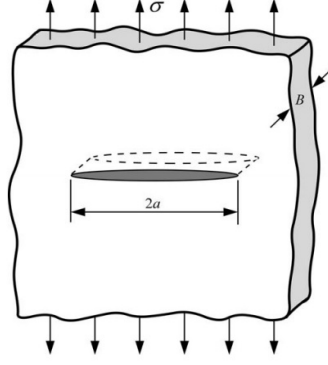


Figure 2.7: Plate with a crack subjected to a tensile stress [1]

balance proposed by Griffith [24] is as follows

$$\frac{dE}{dA} = \frac{d\Pi}{dA} + \frac{dW_s}{dA} = 0 \quad (2.8)$$

$$-\frac{d\Pi}{dA} = \frac{dW_s}{dA} \quad (2.9)$$

Where E is the total energy and Π is the potential energy due to the internal strain energy and external forces and W_s is the work required to create new surfaces. Here, Π is defined as

$$\Pi = \Pi_0 - \frac{\pi\sigma^2 a^2 B}{E} \quad (2.10)$$

Where B is the thickness of the plate and Π_0 is the potential energy of an un-cracked plate. The energy required for the formation of new surface is given as

$$W_s = 4aB\gamma_s \quad (2.11)$$

$$-\frac{d\Pi}{dA} = \frac{\pi\sigma^2 a}{E} \quad (2.12)$$

Where γ_s is the surface energy of the material

$$\frac{dW_s}{dA} = 2\gamma_s \quad (2.13)$$

Solving for fracture stress. We get

$$\sigma_f = \sqrt{\left(\frac{2E\gamma_s}{\pi a}\right)} \quad (2.14)$$

Irwin proposed an energy approach for fracture in which a term called as energy release rate G , which is essentially the energy available for crack extension as

$$G = -\frac{d\Pi}{dA} \quad (2.15)$$

For a wide plate with crack length $2a$. The energy release rate is given as

$$G = \frac{\pi\sigma^2 a}{E} \quad (2.16)$$

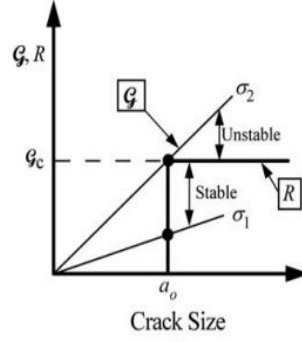


Figure 2.8: Driving force vs. R curve diagram [1]

The Eq. 2.9 gives the energy release rate for linear materials. The definition holds for non-linear elastic materials

$$J = -\frac{d\Pi}{dA} \quad (2.17)$$

Where Π is the potential energy and A is the crack area. The potential energy is given as

$$\Pi = U - F \quad (2.18)$$

U is defined as the strain energy stored in the body and F is the work done by external forces.

For an elastic material, the energy release rate is defined as the potential energy released from a structure when the crack grows in an elastic material. The strain energy stored in elastic plastic material is not released when the crack grows. The crack growth in such materials leaves a plastic deformation. Thus, in elastic plastic materials, the J value in Eq. 2.17 relates the difference in energy absorbed by specimen with neighboring crack sizes.

Stable and unstable crack growth

The crack extension occurs when the energy release rate is equal to the fracture energy, but the crack growth can be both stable and unstable depending on how the energy release rate (G) and fracture energy (w_f) vary. The fracture energy is the resistance to crack growth and is hereby represented as R . The driving force vs R curve is shown in Fig. 2.8. The figure illustrates a material with a flat R-curve, where the resistance offered by the material is constant with crack growth. When stress is σ_1 , the crack growth is stable, however, if the stress is σ_2 the crack growth is unstable since the driving force increases with crack growth, but material resistance remains constant. Rice [22] showed that the value of J integral is equal to the energy release rate in a non-linear elastic body that contains a crack. In the domain of EPFM, the energy available for crack extension is given as

$$J = \frac{d\Pi}{dA} \quad (2.19)$$

Where Π is the potential energy and A is the crack area. The potential energy is given by

$$\Pi = U - F \quad (2.20)$$

Where U and F are the strain energy stored and the work done by external forces respectively

Dynamic crack growth

The study of dynamic fracture mechanics includes three main features that are not present in LEFM and EPFM. They are the inertia force, the rate dependent behaviour of materials and the reflected stress waves. Inertia effects are important when the load value changes or the crack grows rapidly. In these cases, a portion of the work that is applied is converted to kinetic energy. Most metals are not sensitive to strain rates at ambient temperatures. The reflecting stress waves influence the local crack tip and thereby alter the fracture behaviour.

The study of crack growth along interfaces was conducted by A Needleman et al. [25]. The traction separation law is described by them as

$$T = -\frac{\partial\phi}{\partial\Delta} \quad (2.21)$$

The separation process is taken to be elastic so that the traction across the cohesive surface is function of displacement jump. Here, ϕ is the cohesive potential.

Chapter 3

Cohesive zone modelling of cracked interface

3.1 Cohesive Model

Strip yield model

The strip yield model was proposed by Dugdale and Barenblatt. The model assumes compressive stresses at each crack tip. The model assumed a plastic zone of length r as described in the Fig. 3.1. where r is the length of the plastic zone with a compressive stress equal to the yield stress σ_{ys} applied at each crack tip. Mathematically, the stresses at the crack tip are equal to infinity. To overcome this drawback, Dugdale(1960) and Barenblatt(1962) introduced cohesive models. The authors divided the crack into two parts, one part which is stress free and the other is loaded by cohesive stress. The Fig. 3.2 gives the mathematical and actual crack tip, the compressive yield stress is applied on the crack tip. The Dugdale model introduced the cohesive stress as equivalent to yield stress.

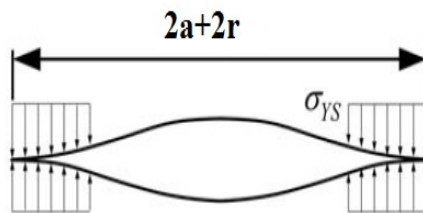


Figure 3.1: The strip yield model [1]

The cohesive zone model helps in explaining the singularity at the crack tip and helps us in representing the crack tip with a physical model. The material separates across the crack and the cohesive forces resist its growth. The quantifying of this phenomenon is done using the traction separation law. Cohesive zone models developed in later stages have been successfully able to predict the fracture behaviors. The model developed by Needleman in 1987 [26] who used a polynomial

law for describing the void nucleation in metals. Xu and Needleman [27] used the exponential cohesive model to study the void nucleation at the interface of particle and matrix material, fast crack growth in brittle materials and the dynamic crack growth along the interface of bimetals. Camacho and Ortiz(1996) [28] selected a linearly decreasing cohesive zone fracture model, this was employed to study multiple cracks along arbitrary cracks during impact damage in brittle materials. Many cohesive models include an initial rising in the traction with an increasing separation, reach a peak and then the traction drops downward which is the softening trend in the traction-separation. Tvergaard and Hutchinson (1992) developed a trapezoidal traction separation function to evaluate crack growth resistance in elasto-plastic materials. Some of the traction separation laws described above are shown in Fig. 3.3.

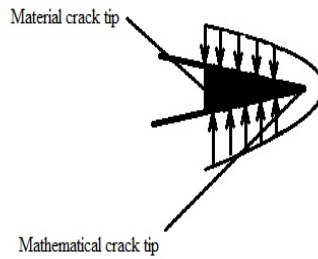


Figure 3.2: Crack tip cohesive model

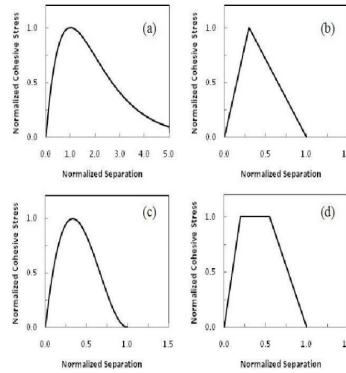


Figure 3.3: Different forms of traction-separation law

Traction Separation Law, TSL

The cohesive law relates the relative motion between the surfaces in contact and is aptly named the traction separation law. Cohesive zone models are used to overcome the stress singularities in linear elastic fracture mechanics. The work done in creating a new surface is not singular and corresponds with the fracture energy and is the area under the traction separation curve.

$$\tau_0 = \int_0^{\delta_0} T(\delta)d\delta \quad (3.1)$$

Material separation is assumed to occur through atomic scale separation i.e cleavage of atomic layers. The cohesive element is shown in Fig. 3.5. The cohesive force acts when the the separation begins and the cohesive force does not act in regions that are completely separated from the second element.

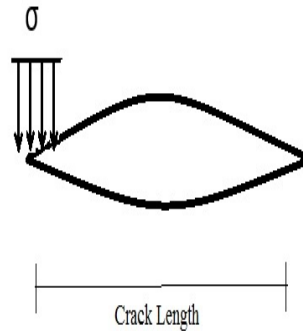


Figure 3.4: Cohesive zone

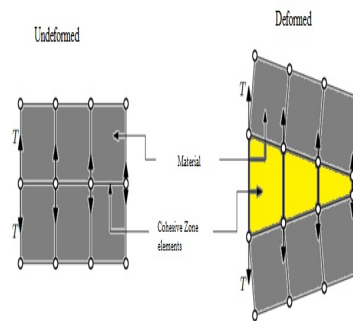


Figure 3.5: Cohesive element

3.2 Modelling

A compact tension specimen was considered for studying the cohesive zone models. The specimen was modelled on the general purpose FE code ABAQUS. The study was conducted on two different sets of cohesive zone models. The linear and the bilinear models. Cohesive elements were embedded in the fracture process zone . The CT specimen was subjected to a mode III anti plane shear load.

3.2.1 Specimen geometry

The CT specimen that was used in the analysis. The CT specimen was modelled according to the ASTM E399 standard [29]. The specimen for the CT specimen is specified in Table 3.1. The CT specimen dimensions are shown in Fig. 3.6.

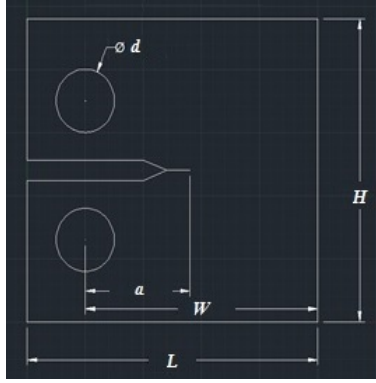


Figure 3.6: Subset matching and deformation tracking in DIC

Table 3.1: CT specimen dimensions with edge crack

Quantity	Value (kJ/mm^2)
Width of specimen, W(mm)	50
Crack length, a (mm)	22.5
Ligament length, b (mm)	27.5
Thickness of specimen, B(mm)	12.5
Diameter of Hole, d(mm)	12.5
Height, H(mm)	60
Length, L(mm)	62.5

Material Properties

The material properties of Al-T6 531 is obtained from uni-axial tensile test on dog-bone specimen using MTS Landmark servo-hydraulic machine of 100 kN capacity. Fig. 3.8 shows the experimental stress-strain curve (solid line) obtained from uni-axial tensile test on dog-bone specimen. Here, ordinate axis represent Cauchy stress in MPa and abscissa represent the strain. The Youngs modulus (E) is obtained from the slope of initial linear region. Yield strength is obtained by drawing a 0.2 percent offset straight line (broken line) that is parallel to the initial straight line portion of the stress-strain curve. The stress level at which the offset straight line intersect the experimentally obtained stress-strain curve is identified as 0.2 percent offset yield strength as shown in Fig. 3.8. The Youngs modulus (E) and yield strength obtained for Al-T6 531 are 70.90 GPa and 440.22 MPa respectively.

3.2.2 Finite Element Model

The finite element analysis of the CT specimen was performed on the commercial FE software ABAQUS 6.9. The CT specimen was modeled according to ASTM E399 [29] standards. The J integral was computed for the 8 separate sections below. The crack was modeled using the cohesive zone. The method required the definition of a cohesive interaction which is described in detail in later sections.

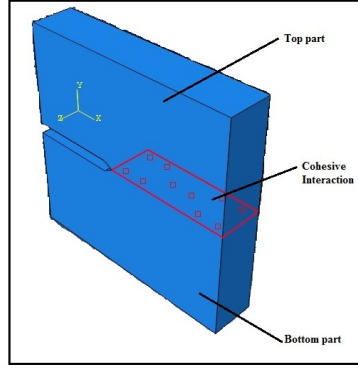


Figure 3.7: Cohesive interaction specified at the point of contact

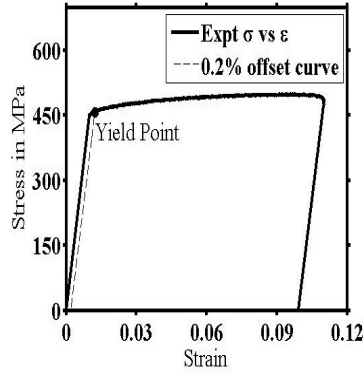


Figure 3.8: Experimental Elasto-Plastic stress strain curve

Finite Element mesh

The CT specimen was modeled using both cohesive elements(COH3D6) and also uses 3D stress elements(C3D8R). The cohesive elements were specified at the area of contact. The mesh at the crack tip use single bias that includes more number of nodes at the crack tip and the number of nodes become lesser as we move away from the crack tip. This was done with a view to capture the singularity.

3.2.3 Cohesive element

For a CT specimen the top and bottom parts are modeled separately as shown in Fig 3.7. In the figure, the highlighted region is specified as a cohesive interaction with damage. The cohesive interaction was defined at the face between the top and bottom parts. The linear and bilinear cohesive traction separation law was specified for different sets of simulations.

The cohesive crack model considers a fracture process zone (FPZ) which exists in front of the real crack tip in the FPZ, energy dissipation occurs. Also, in the FPZ, there exists tractions in the normal (t_n) and tangential directions [4] . The traction separation law is shown in the Fig. 3.10. It shows the critical crack opening displacement δ_{nf} .When the crack initiates a linear-elastic ascending phase exists where the traction increases with increasing displacement. This phase is called the hardening phase. The second phase where the the traction decreases monotonically with the

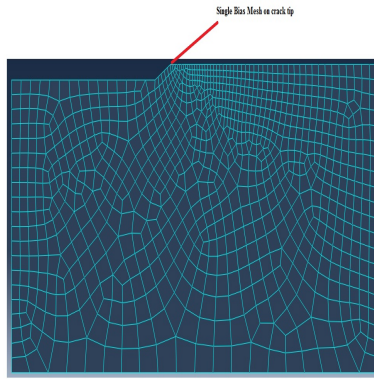


Figure 3.9: Mesh used in crack analysis

increasing displacement. This phase is termed strain softening. The area of the traction separation law for both the linear Fig. 3.11 and bilinear Fig. 3.10 models are the same.

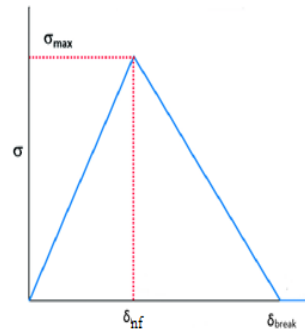


Figure 3.10: Traction separation law for cohesive elements

The cohesive elements were embedded in the region surrounding the crack plane. These cohesive elements were tied with a contact constraint to the surrounding 3D stress elements. The cohesive elements were fitted with the cohesive models to study the response under different conditions.

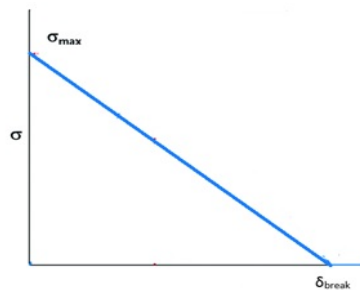


Figure 3.11: Linear traction separation law

3.2.4 Loading

The load applied in the analysis of the CT specimen was of a shear traction on the side edges of the specimen as shown in the Fig. 3.12. The shear traction ensures that there exists a mode III loading in the CT specimen. The other end of the CT specimen was confined in all directions i.e all displacements in X, Y and Z directions and all the rotations were also confined.

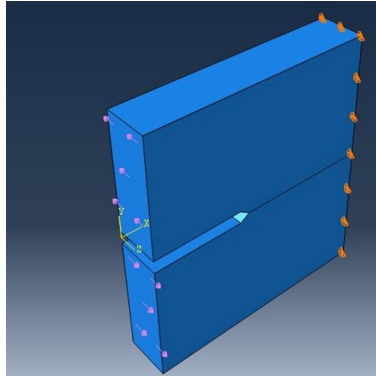


Figure 3.12: Loading for Mode III

3.2.5 Results

The J integral was computed for the different types of analysis. The results are displayed in the following figures

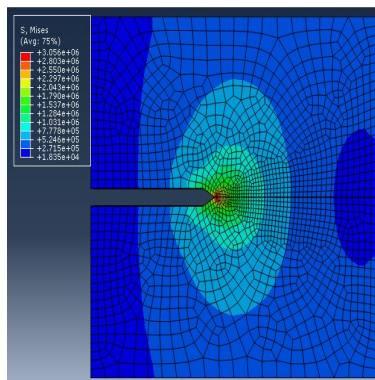


Figure 3.13: Stress plots for Mode III-LEFM The computed J-Integral value was 13.69 kJ/mm^2

The following results were compiled for the linear cohesive zone model

Table 3.2: J integral values at different conditions for linear cohesive zone model

Condition	J integral (kJ/mm^2)
LEFM	13.69
EPFM	15.87
LEFM and dynamic	17.38
EPFM and dynamic	21.54

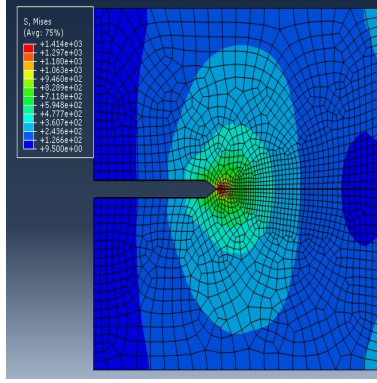


Figure 3.14: Stress plots for Mode III-EPFM The computed J-Integral value was $17.38 \text{ kJ}/\text{mm}^2$

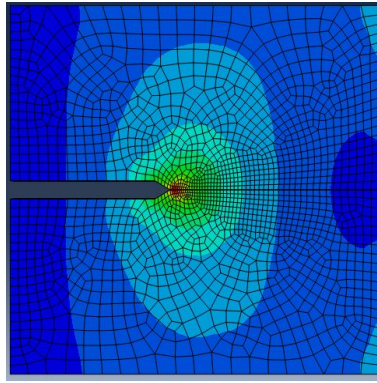


Figure 3.15: Stress plots for Mode III-Dynamic The computed J-Integral value was $15.87 \text{ kJ}/\text{mm}^2$

Table 3.3: J integral values at different conditions for bilinear CZ model

Condition	J integral (kJ/mm^2)
LEFM	13.91
EPFM	16.08
LEFM and dynamic	18.31
EPFM and dynamic	20.68

3.3 Conclusion and Future Scope

The analysis of Compact tension was performed using ABAQUS. The J integral was computed for the eight different cases. The J integral values were obtained from the FE code. The J integral for the EPFM analysis was found to be greater than the one obtained from LEFM. This is due to the fact that in LEFM analysis, the deformations around the crack tip are considered lesser than the crack length, however, this is only applicable in cases where the loads applied are small. Therefore, the J integral values vary in the cases of LEFM and EPFM.

The J integral values were found to be greater in the dynamic case when compared to the EPFM case. This is due to the fact that, the energy release rate during crack extension Δa is decrease in total elastic strain energy and total kinetic energy. The kinetic energy exists because the crack is extending at a finite velocity. Thus the energy is dissipated due to inertial effects also. Thus the J

integral values were found to be larger in case of dynamic crack propagation. The values obtained for the bilinear CZ model were almost similar to the ones obtained from the linear CZ model. This is because the area under the traction-separation curve is constant for both the models adopted. The area under the traction separation curve is equal to energy release rate G_C .

Chapter 4

Crack propagation in bimaterial using spectral methods

4.1 Introduction

The estimates due to failure due to fractures is enormous [30]. Thus the causes and methods to predict these failures can result in saving both human lives and the cost. Fracture mechanics is an area developing area of Engineering that aims to study the damage on structures that are caused by cracks. Dynamic fracture mechanics is the area of fracture mechanics that studies spontaneously propagating cracks.

S lee and Ravichandran [31] also used Homalite 100 in their experiments. They bonded two pieces of Homalite-100 except in the center. They used a central inclined crack configuration and photoelastic fringes were obtained using a high speed camera. They studied the effect of the surface roughness and lateral confinement on the fringe patterns and came to the conclusion that average speed of wing crack was higher in higher coefficient of friction surfaces. The experiments conducted on bimaterial systems by A J Rosakis et al. [32] to study waves generated by the intersonic crack propagation. J Lambros and Rosakis A J [33] have compiled some of the results conducted on dynamically propagating interfacial cracks. One point bend type experiments were conducted on PMMA specimen. P H Geubelle and W G Knauss have taken on the problem of crack growth at interface between two two linearly elastic solids when the conditions that promote crack growth are prevalent [34].

The bimaterial which was made of orthotropic-isotropic material was subjected to a far field tensile loading and was analysed using photoelasticity by Kwanh Ho Lee et al. [35]. They used the photoelasticity technique to study interfacial crack between an isotropic and orthotropic that were subjected to static far-field tensile loading. The fracture parameters for the isotropic-orthotropic bimaterial were studied for static and dynamic crack under mode I load. Roasakis AJ citerosakis1979determination used the elastodynamic crack tip stress field to establish the exact equations of the caustic envelope formed by the reflection of light rays from the surface of a planar solid near the tip of a propagating crack. Arun shukla et al. [36] studied the static and dynamic fracture of interfaces between orthotropic and isotropic materials using photoelasticity. In their study two specimen of different fiber orientations of an edge cracked bi-material specimen were studied. They obtained SIF values

using both experimental methods and also using boundary collocation methods and the results were in close agreement. Chaitanya K Desai et al. [37] studied the delamination of bimaterial interface using Digital Image correlation by finding the displacement fields. They studied center and edge cracked specimen and also four point bend test specimen to find the stress intensity factor using DIC and compared the results with theoretical and/or Finite element computations.

4.1.1 Bimaterial interface

A strip of infinite length is examined for crack propagation in our present study. The strip consists of two materials with material constants E_1, μ_1 and E_2, μ_2 [38]. The bimaterial is essentially two strips of any material joined together by any means such as adhesives or welding etc. The interfaces of bimaterials are often the weakest part of the structure and thereby are an area of paramount interest to Engineers everywhere.

The stress state in homogeneous materials with a crack is quantified using the Stress intensity factor, P P L Matos et al. have [39] developed a method for quantifying the stress intensities in bimaterial fracture.

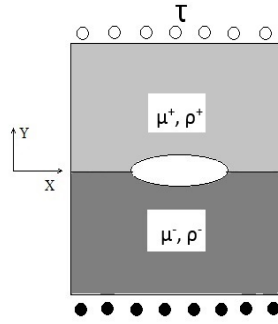


Figure 4.1: Bimaterial subjected to Anti-plane shear

4.1.2 Problem Description

In the present problem, the fracture modes of both the materials were studied separately. The materials were subjected to an anti-plane shear traction. The shear modulus and the density of the material are respectively defined for the top and bottom as μ^+, ρ^+ and μ^-, ρ^- respectively. Where the superscript represents top and bottom surface respectively. The bimaterial was subjected to an anti-plane shear traction.

4.2 Formulation

The spectral formulation involves a Fourier representation, the formulation is done for a bi-material body. A planar crack of arbitrary shape is defined at the interface between two semi-infinite linearly elastic half spaces. The plane of the interface is defined along $x_2 = 0$. The formulation uses an exact Fourier representation between Fourier coefficients for tractions and displacement. The stresses and displacement discontinuities are defined as $\sigma_{ij}(x_1, x_2, x_3, t)$ and $u_i(x_1, x_2)$ respectively.

The histories are of stresses and displacements are related by the two dimensional elastodynamic expression (Cochard and Madariaga,1994)[40].

$$\tau_j(x_1, x_3, t) = \tau^0(x_1, x_3, t) + f(x_1, x_3, t) - \frac{\mu}{2c}\delta(x_1, x_3, t)(1) \quad (4.1)$$

The representation in [41] is in the form of a superposition i.e the sum of a stress applied(τ_j^0). The function $f(x_1, x_3, t)$ are the functions of displacement discontinuities upto the present time. The displacement and functionals respectively are represented in the following form

$$\delta_p(x_1, x_3, t) = D_p(t)e^{(kx_1+mx_3)} \quad (4.2)$$

$$f_q(x_1, x_3, t) = F_q(t)e^{kx_1+mx_3} \quad (4.3)$$

The above equation has separated the displacement which was a function of both time t and space (x_1, x_3) into a product of terms each, one dependent on time and the other dependent on space. The Fourier transform was used for exactly this purpose.

4.2.1 Two-dimensional formulation

The spectral formulation is first established for the two dimensional case where the problem is independent of x_3 . The components of the displacement are expressed as

$$u_1(x_a, t) = \phi_{,1}(x_a, t) + \psi_{,2}(x_a, t); u_2(x_a, t) = \phi_{,2}(x_a, t) - \psi_{,1}(x_a, t) \quad (4.4)$$

where the potentials ϕ and ψ satisfy

$$c_d^2\phi_{,aa} = \phi_{tt} \quad (4.5)$$

$$c_s^2\psi_{,aa} = \psi_{tt} \quad (4.6)$$

The potentials are represented as spectral components as

$$\phi(x_a, t) = e^{iqx_1}\phi_1(x_2, t, q) \quad (4.7)$$

$$\psi(x_a, t) = e^{iqx_1}\psi_1(x_2, t, q) \quad (4.8)$$

$$\Omega(x_a, t) = e^{iqx_1}\Omega_1(x_2, t, q) \quad (4.9)$$

We introduce the Laplace transform for Eq. 4.9

$$c_d^2[-q^2\hat{\phi}(x_2, t, q) + \hat{\phi}''(x_2, t, q)] = p^2\hat{\phi}(x_2, t, q) \quad (4.10)$$

Where the hat represents the Laplace transformed variable. From the above equation, we obtain

$$\hat{\phi}''(x_2, p, q) = q^2\alpha_d^2\hat{\phi}(x_2, p, q) \quad (4.11)$$

$$\hat{\psi}''(x_2, p, q) = q^2\alpha_s^2\hat{\psi}(x_2, p, q) \quad (4.12)$$

$$\hat{\Omega}''(x_2, p, q) = q^2\alpha_d^2\hat{\Omega}(x_2, p, q) \quad (4.13)$$

Where the differentiation is with respect to x_2 Combining the equations and to obtain the laplace transformed displacement field,

$$\hat{u}_1(x_a, p) = e^{iqx_1} [iq\hat{\phi}_0(p, q)e^{-q\alpha_d x_2} - q\alpha_s \hat{\psi}_0(p, q)e^{-q\alpha_s x_2}] \quad (4.14)$$

$$\hat{u}_2(x_a, p) = e^{iqx_1} [-q\alpha_d \hat{\phi}_0(p, q)e^{-q\alpha_d x_2} - iq\hat{\psi}_0(p, q)e^{-q\alpha_s x_2}] \quad (4.15)$$

$$\hat{u}_3(x_a, p) = e^{iqx_2} \hat{\Omega}_0(p, q)e^{-q\alpha_s x_2} \quad (4.16)$$

The tractions and the displacements are required to be found out. The Fourier coefficients $U_j(t, q)$ are defined by

$$\hat{u}_j(x_1, x_2 = 0+, t) = U_j(t, q)e^{iqx_1} \quad (4.17)$$

From the Eq. 4.17 we obtain \hat{U}_1 and \hat{U}_2 . We find the Laplace transformed potentials $\hat{\phi}_0(p, q)$ and $\hat{\psi}_0(p, q)$ as

$$\hat{\phi}_0(p, q) = \frac{-iq\hat{U}_1(p, q) + q\alpha_s \hat{U}_2(p, q)}{q^2(1 - \alpha_s \alpha_d)} \quad (4.18)$$

$$\hat{\psi}_0(p, q) = \frac{iq\alpha_d \hat{U}_1(p, q) + iq\hat{U}_2(p, q)}{q^2(1 - \alpha_s \alpha_d)} \quad (4.19)$$

The $\hat{\phi}_0$ and $\hat{\psi}_0$ are substituted into Eq. 4.16 to obtain the displacement fields \hat{u}_i for the upper half space in terms of the components \hat{U}_i along the top half of the fracture plane i.e $x_2 = 0^+$.

$$\hat{u}_1(x_\alpha, p) = e^{iqx_1} [\hat{U}_1(p; q) \frac{e^{-q\alpha_d x_2} - \alpha_s \alpha_d e^{-q\alpha_s x_2}}{1 - \alpha_s \alpha_d} + \hat{U}_2(p; q) \frac{iq\alpha_s}{q(1 - \alpha_s \alpha_d)} (e^{-q\alpha_d x_2} - e^{-q\alpha_s x_2})] \quad (4.20)$$

$$\hat{u}_2(x_\alpha, p) = e^{iqx_1} [\hat{U}_1(p; q) \frac{iq\alpha_d}{q(1 - \alpha_s \alpha_d)} (e^{-q\alpha_d x_2} - e^{-q\alpha_s x_2}) + \hat{U}_2(p; q) \frac{e^{-q\alpha_s x_2} - \alpha_s \alpha_d e^{-q\alpha_d x_2}}{1 - \alpha_s \alpha_d}] \quad (4.21)$$

The traction components are written in spectral components and obtain expressions for the tractions are obtained from the above expressions.

4.2.2 Spectral Formulation for Mode III

The spectral formulation described above is used for mode I and II type of fracture. The spectral formulation described for mode III is described below. The spectral formulation begins from the linear momentum equation balance. The spectral formulation for mode III crack for a homogeneous material is described by Perrin et al. [42] and the subsequent formulation for a Functionally graded material (FGM) is described by Kulkarni et al. [43].

Formulation for Mode III for bimaterial

For the numerical procedure for Mode III rupture across a bimaterial [44], the length of the crack is chosen as X . The crack propagates along the plane $x_2 = 0$. An anti-plane shear of magnitude τ_0 is applied along the weak plane

$$\frac{\partial \sigma_{13}}{\partial x_1} + \frac{\partial \sigma_{23}}{\partial x_2} = \rho \ddot{u}_3 \quad (4.22)$$

Where σ_{13} and σ_{23} describe the stress components and the u_3 is the out of plane displacement. The kinematic relation for the mode III case is as follows.

$$\sigma_{3\alpha} = \mu(x_2) \frac{\partial u_3}{\partial x_\alpha} \quad (4.23)$$

The α represents the subscript varies from 1 to 2. Combining the above two equations, we obtain the elastodynamic equation in the terms of displacement.

$$u_{3,11} + u_{3,22} = \frac{\ddot{u}_3}{c_s^2} \quad (4.24)$$

Where c_s^2 is the shear wave speed and is obtained as $\sqrt{\frac{\mu}{\rho}}$. The variation for μ and ρ are identical i.e the shear wave speed variation along the length is constant.

The spectral component of Eq. 4.24 and Laplace transform as defined in Eq. 4.25

$$\hat{U}(y, s) = \int_0^\infty e^{-st} U(y, t) dt \quad (4.25)$$

We define the spectral components along the fracture plane as

$$u_3(x_1, x_2 = 0^\pm, t) = u_3^\pm(x_1, t) - U_3^\pm(t, q) e^{iqx_1} \quad (4.26)$$

$$\sigma_{23}(x_1, x_2 = 0, t) = \tau_3(x_1, t) = T_3(t, q) e^{iqx_1} \quad (4.27)$$

The above equation, back in time domain yields The Fourier coefficients of the elastodynamic stress and displacement fields are related in the Laplace domain by

$$\hat{T}_3(p, q) = \mp \mu q \alpha_s^\pm \hat{U}_3^\pm(p, q) \quad (4.28)$$

where $\alpha_s = \sqrt{1 + \frac{p^2}{q^2 c_s^2}}$

4.2.3 Independent Formulation

The elastodynamic response of two half spaces is taken separately.

$$\tau_{3inst}(x_1, t) = \mp \frac{\mu^\mp}{c_s^{mp}} \dot{u}_3(x_1, t) \quad (4.29)$$

We thus rewrite 4.28 as

$$\hat{T}_3(p; q) = \pm \frac{\mu}{c_s^\pm} p \hat{U}_3^\pm(p, q) \mp \mu^\pm q \left(\alpha_s^\pm - \frac{p}{qc_s^\pm} \right) \quad (4.30)$$

Which in the time domain is represented as

$$\tau_3(x_1, t) = \tau_3^0(x_1, t) \mp \frac{\mu^\pm}{c_s^\pm} \dot{u}_3^\pm(x_1, t) + f_3^\pm(x_1, t) \quad (4.31)$$

where the externally applied anti-plane shear traction stress $\tau_3^0(x_1, t)$, the $f_3^\pm(x_1, t)$ represents

the convolution term. The convolution is expressed in the Fourier domain as

$$f_3^\pm(x_1, t) = F_3^\pm(t, q)e^{iqx_1} \quad (4.32)$$

Where the Fourier coefficient, $F_3^\pm(t, q)$ is given as

$$F_3^\pm(t, q) = \mp \mu^\pm q \int_0^t C_{III}^{in}(qc_s^\pm(t-t'))U_3^\pm(t', q)qc_s^\pm dt' \quad (4.33)$$

The convolution term is given as

$$C_{III}^{in} = \frac{J_I(T)}{T} \quad (4.34)$$

Where J_I is the Bessel function The convolution kernel for mode III is plotted in Fig. 4.2. The

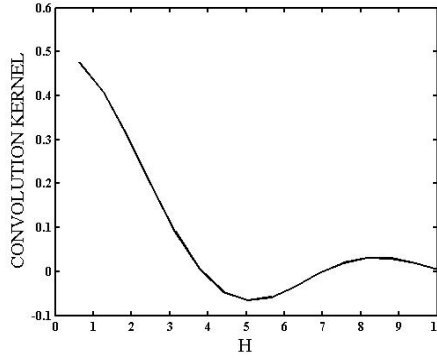


Figure 4.2: Convolution kernel plot for mode III

evolution of each Fourier mode is described by the above elastodynamic relations. We consider an explicit scheme.

$$\delta(x, t + \Delta t) = \delta(x, t) + \Delta \dot{\delta}(x, t) \quad (4.35)$$

Where Δt is the time step. The time step Δt is chosen to be a fraction of the time needed for the shear wave to propagate the smallest distance between the grid points defined on the fracture plane as

$$\Delta t = \beta \frac{\Delta x}{\max(c_s^+, c_s^-)} \quad (4.36)$$

The parameter β is user defined and plays a critical role in the stability and the precision of the numerical scheme. The scope of our present study uses only the linear traction separation law as given by

$$\tau_{str} = f(x, t, \delta, \dot{\delta}) \quad (4.37)$$

$$\tau = \tau_c \left(1 - \frac{\delta}{\delta_c}\right) \quad (4.38)$$

Where τ_c is the fracture strength and δ_c is the critical crack opening displacements, both of which are material properties.

The algorithm for the numerical simulation, for each iteration is written below

1. Update the displacement distributions using 4.35

2. Update the externally applied loads τ_j^0
3. Update the interfacial strength using the cohesive relations 4.38
4. Compute the convolution term for mode III using the relation 4.33
5. Initially, the assumption made is that the interface does not undergo failure and that the half spaces move together at constant velocity away from each other i.e ($u_j^+ = u_j^- = u_j$).The velocity and traction are updated.
6. If failure is detected, the crack propagation is catastrophic, otherwise the iteration is repeated with updated displacements The

4.3 Numerical procedure

4.3.1 Cohesive model

In the above sections, we have derived the relations between the traction stresses τ and the displacement u that exists along the interface between the two materials and the histories. The solutions i.e τ and u are related by a cohesive failure model. We assign at the interface, the tractions as equal due to equilibrium condition at the interface. The separation of the cohesive element is shown in figure 4.3. The cohesive zone modelling is explained in detail in a later section.

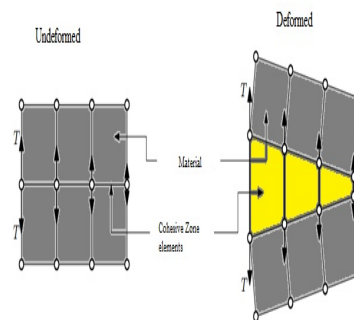


Figure 4.3: Cohesive Element

Chapter 5

Quantification of crack tip parameters using DIC

5.1 Introduction

Crack growth path under both the monotonic static loading and cyclic loading is strongly influenced by the elastic and plastic displacement field at the crack tip. These displacements are governed by a combination of material deformation behavior, and the geometry of the structure [45]. Ahead of crack tip extensive plastic deformation takes places, hence one has to consider elastic-plastic fracture mechanics (EPFM). The crack path is influenced by both elastic and plastic behavior around the crack tip besides other factors. The Jintegral and crack tip opening displacement, δ parameters are used to characterize the crack tip under the domain of EPFM.

Experimentally there are several optical full-field measurement techniques like Photo elasticity, Interferometry, Scanning Electron Microscope (SEM), thermo-elasticity and digital image correlation (DIC) that are used effectively to obtain the elastic displacement field[45, 46]. Among all these methods, DIC technique is more suitable to find out the plastic and anisotropic effects. Further, DIC is user friendly as compared to others. DIC technique was first introduced by Sutton et al. [47]. This technique enables non-contact surface strain measurement of the entire specimen during the test. In this technique, displacement of the subset on the image before and after deformation is matched for determining displacements.

Takamoto Itoh [48] proposed an equation based on the crack opening displacement (COD) for computing J-integral for bi-axially stressed mode I cracks for various inelastic materials. They showed that the J-integral evaluated using their proposed equation is within 25%. Kudari and Kodancha [49] have related the J-integral and the CTOD for compact tension (CT) and single edge notched bend (SENB) specimens. They showed that there exists a linear relationship between J-integral and CTOD. And the proportionality constant was found to depend on the crack length to width ratio and specimen geometry. La Rosa and Marino Cugno [50] have measured the fracture parameters using the digital image correlation technique and we follow some of the techniques suggested in this paper. S Roux et. al. [51] have worked on advanced techniques such as X-DIC (extended DIC) for estimating the stress intensity factors (SIF) for 2D and 3D cracks.

5.2 Digital Image Correlation

Digital image correlation is a non-contact optical-numerical full field measurement technique that facilitates the determination of deformation and strain fields over the specimen surface[52]. The concept of DIC is based on pattern matching wherein the displacement field is identified by correlating images of specimen taken in un-deformed state with the series of images taken in deformed state.

5.2.1 Displacement Mapping

A digital image is essentially a 2-dimensional array of intensity values which can be discretized into small subsets as shown in 5.1. Image correlation works by matching small square subsets of an un-deformed image (5.1(a)) to locations in the image of the surface after deformation (5.1(b)) by means of series of mathematical displacement mapping and cross correlation functions. In 2D DIC, a single camera can be used to provide the in-plane displacement fields. The cross correlation function used to estimate the displacement functions is given by Eq. 5.1

$$C(u, v) = 1 - \frac{\sum_{i=1}^n \sum_{i=1}^n [f(x_i, y_i) - F][g(x'_i, y'_i) - G]}{\sqrt{\sum_{i=1}^n \sum_{i=1}^n [f(x_i, y_i) - F]^2} \sqrt{\sum_{i=1}^n \sum_{i=1}^n [g(x'_i, y'_i) - G]^2}} \quad (5.1)$$

Where $x' = (x + u_0 + \frac{\partial u}{\partial x} dx + \frac{\partial u}{\partial y} dy)$ and $y' = (y + v_0 + \frac{\partial v}{\partial x} dx + \frac{\partial v}{\partial y} dy)$, $f(x_i, y_i)$ and $g(x'_i, y'_i)$ represent the grey levels of reference and deformed images, respectively and (x_i, y_i) , (x'_i, y'_i) are the co-ordinates of a point in the subset before and after deformation respectively. Here, F is mean intensity value of reference subset and G is the mean intensity of deformed subset. And n is the width of the subset in pixel and u_0, v_0 are translations of the centre of the subset in x and y directions respectively. Subset is the area which contains multiple pixels.

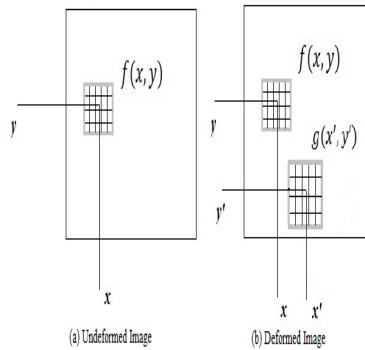


Figure 5.1: Subset matching and deformation tracking in DIC

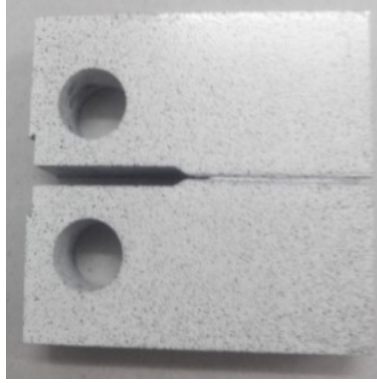


Figure 5.2: Speckled image pattern in CT specimen

5.3 Experimental Procedure

Specimen Preparation

In this study, CT specimen are made of Aluminium T6 531 alloy material. The specimen is cut from 12.5 mm thick Al T6531 alloy sheet according to ASTM E399 standard [29] using electronic wire cut electro discharge machine (EDM). During the machining, pre-crack is done on the CT-specimens using fatigue loading at 10Hz with crack driving force $8MPa$, to simulate the real crack of length a . The schematic diagram of CT-specimen is shown in 5.3 and the specimen dimensions are tabulated in Table 5.1.

Table 5.1: CT specimen dimensions with edge crack

Quantity	Value (kJ/mm^2)
Width of specimen, W(mm)	50
Crack length, a (mm)	22.5
Ligament length, b (mm)	27.5
Thickness of specimen, B(mm)	12.5
Diameter of Hole, d(mm)	12.5
Height, H(mm)	60
Length, L(mm)	62.5

After obtaining the edge cracked CT specimen, surface of the CT specimen is prepared for DIC. To improve the surface adhesion, dust free specimen surface is obtained by cleaning it with isopropyl solution. The speckle pattern on the surface of the specimen is generated by initially creating a white background through spraying acrylic white paint. Followed by random speckle pattern of Carbon black paint (Golden air brush colour) is applied over the dried white background with an Iwata CM-B airbrush (Iwata-Media, Inc.) having a nozzle of 0.5 mm diameter

Material Properties

The material properties of Al-T6 531 is obtained from uni-axial tensile test on dog-bone specimen using MTS Landmark servo-hydraulic machine of 100 kN capacity. Fig. 5.4 shows the experimental stress-strain curve (solid line) obtained from uni-axial tensile test on dog-bone specimen. Here, ordinate axis represent Cauchy stress in MPa and abscissa represent the strain. The Youngs modulus

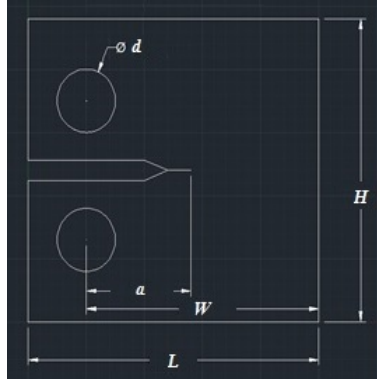


Figure 5.3: Subset matching and deformation tracking in DIC

(E) is obtained from the slope of initial linear region. Yield strength is obtained by drawing a 0.2 percent offset straight line (broken line) that is parallel to the initial straight line portion of the stress-strain curve. The stress level at which the offset straight line intersect the experimentally obtained stress-strain curve is identified as 0.2 percent offset yield strength as shown in Fig. 5.4. The Young's modulus (E) and yield strength obtained for Al-T6 531 are 70.90 GPa and 440.22 MPa respectively.

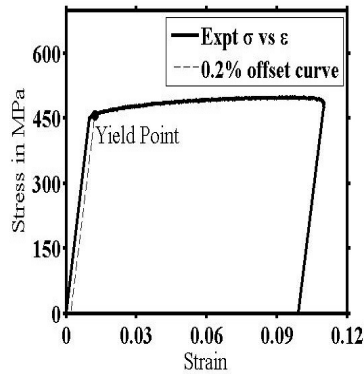


Figure 5.4: Experimental Elasto-Plastic stress strain curve

In plastic region, the power law of Ramberg-Osgood which describes non-linear vs. relationship for strain hardening solid as in equation 5.2.

$$\epsilon = K \left(\frac{\sigma}{\sigma_0} \right)^n \quad (5.2)$$

The plastic strain ϵ is related to stress as $\epsilon \propto \sigma^n$ in which n is the strain hardening exponent. E denotes Young's Modulus, K is material constant and σ_0 is the reference state which can be related to yield stress. The material constants K and n are obtained from the Ramberg-Osgood model.

Using the power-law form of Ramberg-Osgood model in Eq. 5.2 non-linear curve is fitted to the elasto-plastic stress-strain data obtained experimentally using least square fit. The material constants and obtained from Ramberg-Osgood model are tabulated in 5.2.

Table 5.2: Material properties obtained from elasto-plastic stress-strain curve

Material constant	Value (kJ/mm^2)
Young's modulus, E (GPa)	70.90
Offset Yield Strength, σ_0 (MPa)	440.22
Material constant, K	2.4187e+66
Strain hardening exponent, n	31.3325
Poisson's ratio, μ	0.33
Material constant, m	1.79
Length, L (mm)	62.5

5.4 Experimental Setup: DIC

The uni-axial tensile test on CT specimen (see component 6 in Fig5.5) with edge crack was conducted on a computer-controlled MTS Landmark (see component 5 in Fig 5.5) servo-hydraulic machine of 100 kN capacity as shown in Fig. 5.5 The universal testing machine (UTM) is equipped with a standard set of Compact Tension fixtures (see component 7 in Fig.5.5) to grip the specimen. Knife-edges are created at the vertical edge of CT specimen to accommodate a standard COD gauge (see component 8 in Fig.5.5) to measure the crack mouth opening displacement (CMOD).



Figure 5.5: Experimental setup



Figure 5.6: Loaded CT specimen

The experiment is conducted under displacement control mode with displacement rate set to 1

mm per minute. Two halogen light sources (see components 2 & 3 in Fig.5.5) are provided and position of halogen lamps are adjusted to get uniform illumination on the specimen surface. High resolution (2448 x 2048) camera equipped with Tamron lens is used as image capturing system is mounted on a tripod. Tamron lens is used to focus only the region of interest. The feeds from camera and the UTM are connected to image grabbing system (see component 1 in Fig.5.5). Here, laptop is used as the image grabbing system. Vic-Snap commercial software (Correlated Solutions, Inc.) installed in the laptop is used to grab images at a rate of 10/sec

Fig. 5.5 shows the snapshot of DIC experimental setup. Here, the image grabbing system is interfaced to MTS machine via data acquisition card supplied by National Instruments. Fig.5.6 shows the zoomed portion CT specimen attached to the MTS fixtures. Using the pin holes in the CT specimen as shown in Fig. 5.6.

5.5 Fracture Parameters Estimation using Analytical and Numerical Modelling

In this section the fracture parameters of the CT specimen with edge crack is discussed analytically and using XFEM in sections later sections.

5.5.1 Analytical Approach

Stress Intensity Factor (SIF)

The mode-I stress intensity factor K_I is used to predict the stress and displacement field near the crack tip. The magnitude of SIF depends on the sample geometry, the size and location of crack and the applied load. Stress intensity factor for an edge crack in compact tension specimen is obtained from Handbook of Experimental mechanics [53] is shown below in Eq

$$K_I = \frac{P}{BW^{0.5}} P(\alpha) \text{ for } 0.2 \leq \frac{a}{W} \leq 1.0 \quad (5.3)$$

where $\alpha = \frac{a}{W}$, P is the applied load, B is thickness and W is the width of the specimen and,

$$f(\alpha) = \frac{(2 + \alpha)(0.886 + 4.64\alpha - 13.32\alpha^2 + 14.72\alpha^3 - 5.6\alpha^4)^{1.5}}{1 - \alpha} \quad (5.4)$$

5.5.2 J-Integral

The domain of LEFM cannot accurately capture the elasto-plastic fracture behaviour. Hence, based on the small scale yielding, JR Rice [22] in 1968 proposed a new fracture parameter called as J-integral. The magnitude of J-integral represents the non-linear energy release rate due to crack. They have also shown that J-integral is path independent. Hence, it can be evaluated for any path for given loading condition and its functional form is expressed in Eq. 5.5 The schematic in Fig.5.7 represents a typical edge crack under uniaxial loading with a contour .

$$J = \oint_{\Gamma} (W dy - T_i \frac{\partial u_i}{\partial x} ds) \quad (5.5)$$

Where, W is the strain energy density, T_i is the component of traction vector, and τ is closed contour. For estimating J it is separated into elastic and plastic components [1] as shown in Eqn 5.6

$$J = J_{pl} + J_{el} \quad (5.6)$$

The crack tip energy integral is path independent as the material enclosed by the contour is homogeneous. For elastic solids, $J_{el} = G$ contour integral gives the crack tip energy release rate [23]

$$J_{pl} = \frac{\eta_{pl} A_{pl}}{Bb}, \quad \eta_{pl} = 2 + 0.522 * \frac{b}{W} \quad (5.7)$$

Here η_{pl} is the plastic eta factor, B is the specimen thickness, A_{pl} is the area under the Load-CMOD curve, b is the uncrack length, W is the width of the specimen.

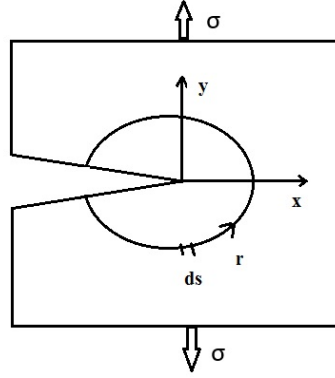


Figure 5.7: J Integral

$$J_{el} = G = \frac{K_I^2}{E'} \quad (5.8)$$

Where, E is Young's modulus and μ is Poisson's ratio

$$J_{pl} = \frac{\eta_{pl} A_{pl}}{Bb} \eta_{pl} = 2 + 0.355 * \frac{b}{W} \quad (5.9)$$

Where, η_{pl} is the plastic eta factor, B is the specimen thickness A_{pl} is the area under the load $CMOD_{pl}$ the uncracked length, W is the width of specimen

5.5.3 Crack Tip Opening Displacement(δ)

In addition to J-integral described above, another important fracture parameter in EPFM is the crack-tip opening displacement (CTOD, δ). The general relation between J-integral and δ is defined by Shih [54] as shown below in 5.10

$$J = m\sigma_y\delta \text{ and } m = 2.685\frac{1}{n} + 1.705 \quad (5.10)$$

Where σ_y is the yield stress of the material, m is the material constant obtained from [55, 56] and n is the strain hardening coefficient(see Table 5.2) Shih [54] haas obtained a relationship between J

and δ 5.11 theoretically by using Hutchinson Rice and Rosengren(HRR) stress fields [23]

$$\delta = d_n \frac{1}{\sigma_y} \text{ and } d_n = \frac{1}{n} \quad (5.11)$$

Where d_n is the constant which depends on Ramberg-Osgood(R-O) material constant m

Further, the CTOD is split into elastic and plastic part [1]. The elastic portion of crack tip opening displacement is related to linear elastic SIF, K [56] and it is given by Eqn 5.12

$$CTOD_{el} = \frac{K_I^2(1 - \mu^2)}{mE\sigma_y} \quad (5.12)$$

Where m is the material constant, σ_y is the Yield strength, E is the Young's Modulus and μ is the Poisson's ratio. The above mentioned parameters are obtained from Table 5.2. Kirk and Dodds[55] and Panontin [56] have obtained the $CTOD_{pl}$ using J_{pl} as given in Eq. 5.13. Using this approach the crack tip opening due to plasticity is computed using the present work.

$$CTOD_{pl} = \frac{\eta_{pl}A_{pl}}{Bbm\sigma_{flow}} \quad (5.13)$$

Where σ_{flow} is flow stress for Ramberg-Osgood model is found out using [55][56] as shown below 5.14

$$\sigma_{flow} = \frac{\sigma_0}{2(X(n) + 1)} \text{ and } X(n) = \frac{\frac{E}{\sigma_0 n} \frac{1}{n}}{e^{\frac{1}{n}}} \quad (5.14)$$

5.6 Numerical analysis

The numerical analysis is done using the general purpose commercial FEM software, ABAQUS 6.9. Figure 5.8 shows CT-specimen modelled as per the ASTM E399 standard with dimensions listed in Table 5.3. Extended finite element method is used to model the crack, hexahedral C3D8R element type is used to create a mapped mesh. Full integration is used with C3D8R element type. The finite element mesh shown in Fig.5.8 has 89321 elements and 186269 nodes. The model is loaded using pin holes. To simulate pin loading, two rigid pins are modelled tied to the pin holes of the CT specimen . A vertical load of 13.69kN is applied on the top pin. While the bottom pins is constrained for all the displacements. Further, x-displacement is constrained along the vertical edge of the left end of the specimen to simulate the constraints due to MTS fixture. And y and z displacement is constrained along the bottom edge to arrest the rigid body displacements.

5.7 Results

5.7.1 Analytical Results

Figure 5.9 shows the load versus CMOD curve obtained experimentally through the COD gauge mounted to the knife edges of CT specimen, which is fed to UTM. In Fig 5.9y-axis represents the load obtained from load cells and x-axis represents the CMOD obtained from the COD gauges mounted to the knife edges of CT specimen as discussed in earlier section.The load vs CMOD in Fig.

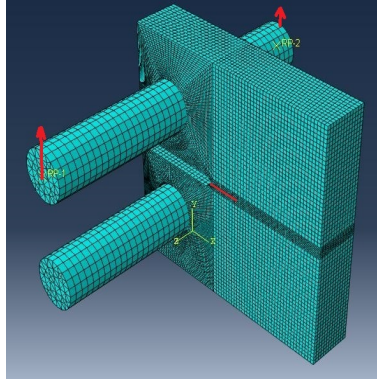


Figure 5.8: Meshed CT specimen

5.9 classified in to Type-1 [1] behaviour and shows slight deviation from linearity before reaching the ultimate failure load P_{Max} . A 5% Secant Line is drawn to determine P_5 . Since the curve represents the Type-I, the critical load $P_Q = P_5$. This deviation in linearity is caused due to the plasticity subcritical crack growth and/or both. Using the area under the load vs CMOD $P_Q P_{Max}$ gives A_{pl} which is later used to obtain the J_{pl} and $CTOD_{pl}$ using the Eqs (5.9,5.13)

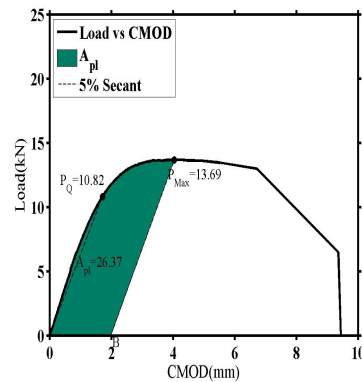


Figure 5.9: Load vs. CMOD

5.7.2 Experimental results

Using the procedure described in earlier sections displacements and strain fields are obtained for Al-T6 531 CT specimen with edge crack using 2D-DIC technique. Figures 5.10 and 5.11 shows the strain ϵ_{yy} at a load level of 13.69 kN (at critical load P_Q , see). The contour plot obtained by post processing the acquired speckle pattern images through VIC-2D 2010 commercial software by Correlated Systems using subset size of 29x29 pixels and a step size of 7. The fracture parameters $CTOD$ and SIF are found from displacements contours ahead of the crack tip using the COD tool featured in VIC-2D 2010 software at various load levels. Figure 5.11 contour plot represents negative ϵ_{xx} ahead of crack tip would assist the crack blunting. The contour shape of the Figures 5.11 and 5.10 represents a typical plane strain plastic zone shape.

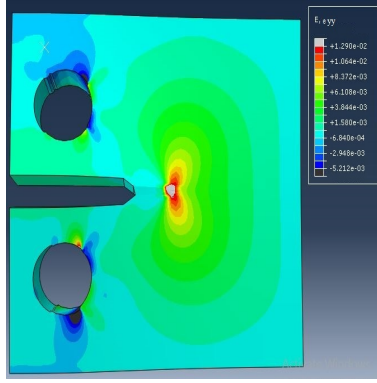


Figure 5.10: Strain plot obtained from FE software

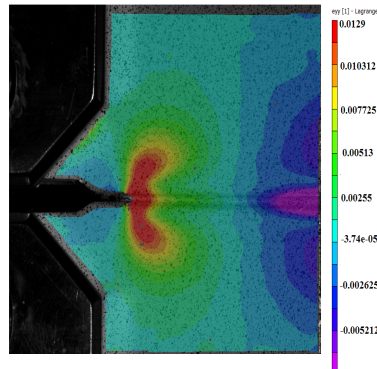


Figure 5.11: Strain plots from DIC

5.7.3 Numerical analysis results

Using FE-model discussed in the earlier section, J-integral is obtained for CT specimen (see Fig.5.8) with different ligament length numerically using XFEM simulation in ABAQUS and plotted J-integral vs ligament length in the Fig. 10(a). Ligament size is the uncrack length of the specimen. It is observed that with the increase in ligament size (i.e. increase in crack length a) J-integral drops in a bilinear fashion. The J-integral near to the crack tip is more dominant because of plastic region ahead of crack tip and further elastic region started in which is dominant. By comparing Load versus CTOD plot as shown in Fig. 10(b), it is come to know that results obtained from both the methods are identical up to the yield. As crack is dependent on load, and when load increases, crack grows faster and further crack opening displacement increases. From both the methods, DIC gives the efficient results.

Table 5.3 summarises the fracture parameters obtained from analytical, experimental and numerical methods for the edge cracked CT specimen made up of Al-T6 531 material. Reasonable match is observed in both elastic parameter (error within 4%) and the plastic parameters J-integral and CTOD (error 5.3% and 17% respectively) between the values obtained through DIC experiment and the XFEM simulation. However, the analytical estimates are far off from both experiments and numerical approach as the constraint from the fixtures are not accounted while making the estimates in the analytical approach.

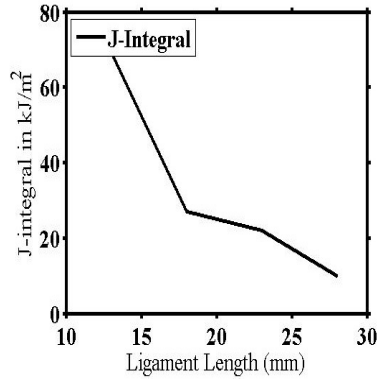


Figure 5.12: J Integral vs Ligament length

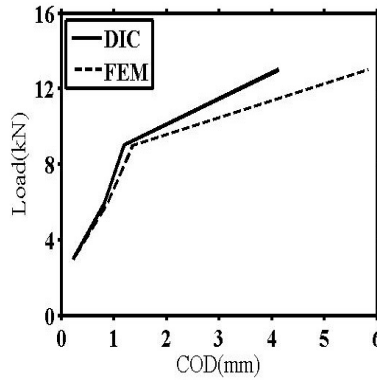


Figure 5.13: Load vs COD

5.8 Conclusion

Fracture parameters such as stress intensity factor (SIF) J-integral and CTOD are obtained for CT specimen using DIC technique. DIC technique is made up Al-T6 531 containing an edge crack. Experimentally, analytically and numerically were found to be close. The relation between J-integral and the crack opening displacement was found to depend upon the method of estimation, specimen geometry and also the aspect ratio. The variation of the J-integral with the ligament length was also obtained using XFEM and the J-integral value in elastic region is found to be linearly decreasing with increase in ligament length. It was observed that value of J-integral is dependent on crack length. Ramberg-Osgood model is fitted for getting non-linear stress-strain relationship and material constants are estimated. DIC technique is more efficient than conventional methods because it is sophisticated technique and simply gives the value of crack tip opening displacement at corresponding load. The J-integral and the CTOD values estimated from the analytical and numerical method were found to be close to the experimental values.

Table 5.3: Fracture parameters for Al T6 531 edge cracked CT specimen

Fracture Parameters	Analytical	DIC	Numerical
SIF $K_I MPa\sqrt{m}$	40.84	67.48	32.56
$J_{IC}(kJ/mm^2)$	196.46	230.19	17.256
CTOD(mm)	0.928	0.961	1.022

References

- [1] T. L. Anderson and T. Anderson. Fracture mechanics: fundamentals and applications. CRC press, 2005.
- [2] N. Chandra. Evaluation of interfacial fracture toughness using cohesive zone model. *Composites Part A: applied science and manufacturing* 33, (2002) 1433–1447.
- [3] R. P. Singh and V. Parameswaran. An experimental investigation of dynamic crack propagation in a brittle material reinforced with a ductile layer. *Optics and lasers in engineering* 40, (2003) 289–306.
- [4] X. Su, Z. Yang, and G. Liu. Finite element modelling of complex 3D static and dynamic crack propagation by embedding cohesive elements in Abaqus. *Acta Mechanica Solida Sinica* 23, (2010) 271–282.
- [5] C. Guo and C. Sun. Dynamic mode-I crack-propagation in a carbon/epoxy composite. *Composites Science and Technology* 58, (1998) 1405–1410.
- [6] D. W. Spring and G. H. Paulino. A growing library of three-dimensional cohesive elements for use in ABAQUS. *Engineering Fracture Mechanics* 126, (2014) 190–216.
- [7] C. Sciammarella and O. Combet. An elasto-plastic analysis of the crack tip field in a compact tension specimen. *Engineering fracture mechanics* 55, (1996) 209–222.
- [8] Y. Lei. Finite element crack closure analysis of a compact tension specimen. *International Journal of Fatigue* 30, (2008) 21–31.
- [9] J. Ožbolt, J. Bošnjak, and E. Sola. Dynamic fracture of concrete compact tension specimen: Experimental and numerical study. *International Journal of Solids and Structures* 50, (2013) 4270–4278.
- [10] A. Turon, C. G. Davila, P. P. Camanho, and J. Costa. An engineering solution for mesh size effects in the simulation of delamination using cohesive zone models. *Engineering fracture mechanics* 74, (2007) 1665–1682.
- [11] J. Williams and H. Hadavinia. Analytical solutions for cohesive zone models. *Journal of the Mechanics and Physics of Solids* 50, (2002) 809–825.
- [12] V. Tvergaard. Crack growth predictions by cohesive zone model for ductile fracture. *Journal of the Mechanics and Physics of Solids* 49, (2001) 2191–2207.

- [13] H. Li and N. Chandra. Analysis of crack growth and crack-tip plasticity in ductile materials using cohesive zone models. *International Journal of Plasticity* 19, (2003) 849–882.
- [14] A. Cornec, I. Scheider, and K.-H. Schwalbe. On the practical application of the cohesive model. *Engineering Fracture Mechanics* 70, (2003) 1963–1987.
- [15] I. Scheider, M. Schödel, W. Brocks, and W. Schönfeld. Crack propagation analyses with CTOA and cohesive model: Comparison and experimental validation. *Engineering Fracture Mechanics* 73, (2006) 252–263.
- [16] W. Li and T. Siegmund. An analysis of crack growth in thin-sheet metal via a cohesive zone model. *Engineering Fracture Mechanics* 69, (2002) 2073–2093.
- [17] I. Scheider and W. Brocks. Simulation of cup–cone fracture using the cohesive model. *Engineering Fracture Mechanics* 70, (2003) 1943–1961.
- [18] V. Tvergaard. Predictions of mixed mode interface crack growth using a cohesive zone model for ductile fracture. *Journal of the Mechanics and Physics of Solids* 52, (2004) 925–940.
- [19] V. Tvergaard. Cohesive zone representations of failure between elastic or rigid solids and ductile solids. *Engineering Fracture Mechanics* 70, (2003) 1859–1868.
- [20] W. Zhang and X. Deng. Asymptotic fields around an interfacial crack with a cohesive zone ahead of the crack tip. *International journal of solids and structures* 43, (2006) 2989–3005.
- [21] W. Zhang and X. Deng. Elastic fields around the cohesive zone of a mode III crack perpendicular to a bimaterial interface. *Journal of Applied Mechanics* 74, (2007) 1049–1052.
- [22] J. R. Rice. A path independent integral and the approximate analysis of strain concentration by notches and cracks. *Journal of applied mechanics* 35, (1968) 379–386.
- [23] J. Rice and G. Rosengren. Plane strain deformation near a crack tip in a power-law hardening material. *Journal of the Mechanics and Physics of Solids* 16, (1968) 1–12.
- [24] A. A. Griffith. The phenomena of rupture and flow in solids. *Philosophical transactions of the royal society of london. Series A, containing papers of a mathematical or physical character* 163–198.
- [25] A. Needlemana, D. Cokerb, and A. Rosakisc. Fast crack growth along interfaces. *Latin American Journal of Solids and Structures* 2, (2005) 5–15.
- [26] A. Needleman. A continuum model for void nucleation by inclusion debonding. *Journal of applied mechanics* 54, (1987) 525–531.
- [27] X.-P. Xu and A. Needleman. Numerical simulations of fast crack growth in brittle solids. *J Mech Phys Solids* 1, (1992) 37.
- [28] G. T. Camacho and M. Ortiz. Computational modelling of impact damage in brittle materials. *International Journal of solids and structures* 33, (1996) 2899–2938.
- [29] A. E399-06. Standard Test Method for Linear-Elastic Plane-strain Fracture Toughness of Metallic Materials. *Annual Book of ASTM Standards, Section 3, Volume 03.01* 520–551.

- [30] D. Roylance. Introduction to fracture mechanics. *Department of Materials Science and Engineering, Massachusetts Institute of Technology* .
- [31] S. Lee and G. Ravichandran. An investigation of cracking in brittle solids under dynamic compression using photoelasticity. *Optics and lasers in engineering* 40, (2003) 341–352.
- [32] A. J. Rosakis, O. Samudrala, R. P. Singh, and A. Shukla. Intersonic crack propagation in bimaterial systems. *Journal of the Mechanics and Physics of Solids* 46, (1998) 1789–1814.
- [33] J. Lambros and A. Rosakis. Dynamic decohesion of bimaterials: experimental observations and failure criteria. *International Journal of Solids and Structures* 32, (1995) 2677–2702.
- [34] P. Geubelle and W. Knauss. Crack propagation at and near bimaterial interfaces: linear analysis. *Journal of applied mechanics* 61, (1994) 560–566.
- [35] K. H. Lee, A. Shukla, V. Parameswaran, V. Chalivendra, and J. S. Hawong. Static and dynamic fracture analysis for the interface crack of isotropic-orthotropic bimaterial. *KSME international journal* 16, (2002) 165–174.
- [36] A. Shukla, V. B. Chalivendra, V. Parameswaran, and K. H. Lee. Photoelastic investigation of interfacial fracture between orthotropic and isotropic materials. *Optics and lasers in engineering* 40, (2003) 307–324.
- [37] C. K. Desai, S. Basu, and V. Parameswaran. Determination of complex stress intensity factor for a crack in a bimaterial interface using digital image correlation. *Optics and Lasers in Engineering* 50, (2012) 1423–1430.
- [38] S. Boere and P. Schreurs. Bimaterial Interface Cracks .
- [39] P. Matos, R. McMeeking, P. Charalambides, and M. Drory. A method for calculating stress intensities in bimaterial fracture. *International Journal of Fracture* 40, (1989) 235–254.
- [40] A. Cochard and R. Madariaga. Dynamic faulting under rate-dependent friction. *Pure and Applied Geophysics* 142, (1994) 419–445.
- [41] P. H. Geubelle and J. R. Rice. A spectral method for three-dimensional elastodynamic fracture problems. *Journal of the Mechanics and Physics of Solids* 43, (1995) 1791–1824.
- [42] G. Perrin, J. R. Rice, and G. Zheng. Self-healing slip pulse on a frictional surface. *Journal of the Mechanics and Physics of Solids* 43, (1995) 1461–1495.
- [43] M. Kulkarni, S. Pal, and D. Kubair. Mode-3 spontaneous crack propagation in unsymmetric functionally graded materials. *International journal of solids and structures* 44, (2007) 229–241.
- [44] P. H. Geubelle and M. S. Breitenfeld. Numerical analysis of dynamic debonding under anti-plane shear loading. *International Journal of Fracture* 85, (1997) 265–282.
- [45] J. Yates, M. Zanganeh, and Y. Tai. Quantifying crack tip displacement fields with DIC. *Engineering Fracture Mechanics* 77, (2010) 2063–2076.
- [46] T. Keating, P. Wolf, and F. Scarpace. An improved method of digital image correlation. *Photogrammetric Engineering and Remote Sensing* 41.

- [47] M. Sutton, W. Wolters, W. Peters, W. Ranson, and S. McNeill. Determination of displacements using an improved digital correlation method. *Image and vision computing* 1, (1983) 133–139.
- [48] T. Itoh. J-integral estimate for biaxially stressed Mode I cracks based on COD strain. *International journal of fatigue* 21, (1999) 1087–1097.
- [49] S. Kudari and K. Kodancha. On the relationship between J-integral and CTOD for CT and SENB specimens. *Fracture and Structural Integrity* pages–3.
- [50] G. La Rosa, A. Marino, and C. Garrano. Fracture mechanics parameters evaluation using the digital image correlation technique: a first approach. In CONVEGNO IGF XXII ROMA 2013. 2013 .
- [51] S. Roux, J. Réthoré, and F. Hild. Digital image correlation and fracture: an advanced technique for estimating stress intensity factors of 2D and 3D cracks. *Journal of Physics D: Applied Physics* 42, (2009) 214,004.
- [52] M. A. Sutton, J. J. Orteu, and H. Schreier. Image correlation for shape, motion and deformation measurements: basic concepts, theory and applications. Springer Science & Business Media, 2009.
- [53] A. KOBAYASHI. Handbook on experimental mechanics. *Englewood Cliffs, NJ, Prentice-Hall, Inc., 1987, 1020* .
- [54] C. Shih. J-Integral estimates for strain hardening materials in antiplane shear using fully plastic solutions. *Mechanics of crack growth* 590, (1976) 1.
- [55] M. T. Kirk and H. Robert. J and CTOD estimation equations for shallow cracks in single edge notch bend specimens. Technical Report, DTIC Document 1993.
- [56] T. Panontin, A. Makino, and J. Williams. Crack tip opening displacement estimation formulae for C (T) specimens. *Engineering Fracture Mechanics* 67, (2000) 293–301.